Journal of Luminescence 161 (2015) 306–312

Contents lists available at ScienceDirect

Journal of Luminescence

journal homepage: www.elsevier.com/locate/jlumin

Luminescence and thermal lensing characterization of singly Eu^{3+} and Tm^{3+} doped Y_2O_3 transparent ceramics

P.Y. Poma [a], K. Upendra Kumar [a], M.V.D. Vermelho [a], K. Serivalsatit [b,c,d], S.A. Roberts [c], C.J. Kucera [c], J. Ballato [b,c], L.G. Jacobsohn [b,c,*], C. Jacinto [a,**]

[a] Grupo de Fotônica e Fluidos Complexos, Instituto de Física, Universidade Federal de Alagoas, Maceió, Alagoas 57072-900, Brazil
[b] Department of Materials Science and Engineering, Clemson University, Clemson, SC 29634, USA
[c] Center for Optical Materials Science and Engineering Technologies (COMSET), Clemson University, Anderson, SC 29625, USA
[d] Research Unit of Advanced Ceramics, Department of Materials Science, Faculty of Science, Chulalongkorn University, Bangkok, Thailand

ARTICLE INFO

Article history:
Received 21 July 2014
Received in revised form
3 January 2015
Accepted 5 January 2015
Available online 13 January 2015

Keywords:
Y_2O_3 ceramic
Eu^{3+} and Tm^{3+} dopants
Judd–Ofelt analysis
Thermal lensing
Thermal conductivity
Fluorescence quantum efficiency

ABSTRACT

Transparent Y_2O_3 ceramics singly-doped with either Eu^{3+} or Tm^{3+} were fabricated by means of sequential consolidation steps at high pressure and temperature. These ceramics were characterized for their luminescence and thermal lensing behaviors, and the results compared to data on single crystals reported in literature. Thermal diffusivity, D, and conductivity, K, values of $D=26\times10^{-3}$ cm^2/s and $K=5.8$ W/m K, respectively, for 1.0 mol% Eu^{3+} and 0.5 mol% Tm^{3+} singly-doped Y_2O_3 transparent ceramics were obtained. These values are about half of those for single crystal analogs. A small temperature coefficient of the optical path length change, $ds/dT=3\times10^{-6}$ K^{-1}, was determined, making these materials suitable for applications requiring nearly athermal response. Selected spectroscopic properties were obtained by means of Judd–Ofelt analysis and together with thermal lens results provided absolute values for the fluorescence quantum efficiency of several levels, particularly 62% for the $^5D_0$ level of Eu^{3+} and 84% for the $^3F_4$ level of Tm^{3+}.

1. Introduction

Rare earths (REs) are widely used as luminescence activators in photonic and optoelectronic materials because their electronic transitions can generate intense emissions of light. The luminescence of triply ionized RE ions commonly presents sharp and intense emission lines. These emissions are almost independent of the chemical environment due to shielding of the 4f electrons by the outer filled 5s and 5p shells, though crystal field splitting effects can be observed. A major exception occurs for the 5d–4f transition of Ce^{3+} that finds application in scintillators where strong electron–host coupling makes this radiative transition span from ultra-violet to red, depending on the host [1].

REs have been incorporated in all types of optical materials, particularly in transparent ceramics [2–5]. The field of transparent ceramics started in the 1960s with the development of translucent Al_2O_3 for lighting applications [6–8], and slowly expanded into other areas, including transparent armor [9], infrared windows [9], lasers [10,11], and scintillators [12]. In the mid-1980s, the first transparent ceramic scintillators, RE-doped $(YGd)_2O_3$ [13] and Gd_2O_2S [14,15], were introduced. These scintillators found enormous commercial success as radiation sensors in computed tomography (CT) scanners [16,17]. As a gain medium for lasers, beyond initial successes in the 1960s and 1970s, transparent ceramic-based lasers achieved broader visibility in mid-1990s with the development of highly transparent $Y_3Al_5O_{12}$:Nd (YAG:Nd) [18–20].

Sesquioxides such as yttria can be easily doped with REs and in general have higher thermal conductivity than that of YAG, making them attractive for high-power laser systems. Since their elevated melting temperature hinders the conventional melt-growth of single crystals, considerable effort has been recently devoted to the development of RE-doped sesquioxide transparent ceramics, particularly RE-doped Y_2O_3 [21–29]. Y_2O_3 is an attractive host for REs due to its 5.6 eV band gap, its high refractive index in the visible region of the spectrum, and low phonon energy of only 430 cm^{-1} that is considerably lower than that of YAG (700 cm^{-1}). Recently, Y_2O_3:RE has also attracted the attention as a scintillator and others [30–35]. Regarding the nano-grained yttria ceramic ($d<100$ nm), in principle it should show

* Corresponding author at: Department of Materials Science and Engineering, Clemson University, Clemson, SC 29634, USA.
** Corresponding author.
E-mail addresses: luiz@clemson.edu (L.G. Jacobsohn), cjacinto@fis.ufal.br (C. Jacinto).

http://dx.doi.org/10.1016/j.jlumin.2015.01.003
0022-2313/

much better mechanical properties in comparison with micro-sized analogs and it should also present better optical transparency due to negligible weak light scattering on randomly oriented nanograins and pores of negligible sizes when compared to the visible light wavelength. When the particle size reduces to nanometer level, their bonding characteristics deviate from those of bulk materials, opening opportunities to manipulate the surface-to-volume ratio. In addition, different morphologies such as rods, wires, thin films, and fibers at the nanoscale have been exploited. However, obtaining pore-free transparent ceramics is not an easy task and this fact is likely the reason for only few works describing obtaining of dense Y_2O_3 nanostructured ceramics [29,34,35]. In this work, the thermo-optical properties of singly Eu^{3+} and Tm^{3+} doped Y_2O_3 transparent ceramics are investigated and compared with single crystal analogs reported in the literature.

2. Experimental procedures

The fabrication of the Y_2O_3:RE transparent ceramics reported herein was achieved through multiple consolidation steps at high pressure and/or temperature of starting nanopowders as described briefly below [27]. The starting nanopowders were prepared by a coprecipitation method using ammonium hydroxide as the precipitant. The yttrium nitrate solution was prepared by dissolving yttrium nitrate hexahydrate (99.9%, Acros Organics) and the RE nitrate hydrate (0.5 mol% for Tm, and 1.0 mol% for Eu; both 99.9%, Acros Organics) in ultrapure water. A 5 mol% solution of ammonium sulfate (99.99%, Sigma Aldrich) was added to the nitrate solution and a 2 M ammonium hydroxide (Certified A.C.S. Plus, Fisher Scientific) solution was added drop-wise in order to precipitate an RE-doped yttrium nitrate precursor. The precipitated precursor was maintained for 3 h at room temperature and then washed twice with ultrapure water and ethanol. The precipitate was dried at 60 °C overnight in vacuum, and calcined at 1050 °C for 4 h under oxygen flowing at 3 l/min to yield RE-doped Y_2O_3 nanopowders. The calcined nanopowders were uniaxially pressed into pellets at approximately 15 MPa without any binder, followed by cold isostatically pressing at 206 MPa. These pellets were sintered in vacuum using a two-step sintering method [36] that consisted of heating to 1500 °C with a heating rate of 10 °C/min and immediately cooling down to 1400 °C, where the samples were kept for 20 h. In order to obtain transparent ceramics, pellets were subsequently hot isostatically pressed at 1300 °C under an argon pressure of 206 MPa for 3 h. After polishing to optical grade, the thicknesses of the 1 cm diameter Y_2O_3:Eu and Y_2O_3:Tm transparent ceramics were 0.7 mm and 0.5 mm, respectively (cf. Refs. [26,27] for photographs).

Luminescence measurements were performed using an Ar laser tuned to a wavelength of 465 nm, with the emission being collected by an optical fiber connected to a McPherson monochromator model 207. The signal was detected using a silicon photodiode model S-010-TE2-H (Electro-Optical Systems) and amplified with a lock-in amplifier SR530 (Stanford Research Systems). Spectroscopic lifetime values were obtained from the analysis of the decay curves using single exponential fitting and linear fitting of log–log plots, and for the nonlinear cases a double exponential adjustment was employed. The detectors used in the lifetime measurements have rise time of < 5 μs (silicon detector), comparable to the cut-off time of the modulation. Absorption spectra were obtained using a PerkinElmer spectrophotometer model Lambda 1050.

The thermal lens (TL) measurements were carried out in the dual beam mode-mismatched configuration using an Ar^+ laser as the excitation and a He–Ne laser tuned at 632.8 nm as the probe beam. For Y_2O_3:Eu the excitation was tuned at 457 nm while for Y_2O_3:Tm it was at 476 nm.

3. Theoretical background

The optical absorption spectra of RE^{3+} ions serve as a basis for understanding their spectroscopic properties. Intensities of the absorption bands are usually expressed in terms of oscillator strengths (f) which are statistically weighted to account for the degeneracy of the initial state. Classically, the oscillator strength represents the number of electric dipole oscillators stimulated by the incoming radiation. It is a measure of the strength of a transition and corresponds to the ratio of the actual intensity to the intensity radiated by one electron oscillating harmonically in three dimensions. Experimentally, the oscillator strength of an absorption transition (f_{exp}) is directly proportional to the area under the absorption curve and is given by [37] $f_{exp} = (mc/\pi e^2 N)\int \alpha(\nu)d\nu$, where $\alpha(\nu)$ is the linear absorption coefficient, ν is the frequency, and N is the RE ion concentration. The majority of the $4f^n$ intraconfigurational transitions corresponds to induced electric dipole (ED) transitions, though some contain both induced ED and magnetic dipole (MD) contributions. In this case, the experimental oscillator strength is calculated by summing the oscillator strength of both types of transitions [38].

According to the Judd–Ofelt (JO) theory [39,40], the oscillator strength for an induced ED transition from the ground state, ΨJ, to an excited state, $\Psi' J'$, assuming that all the crystal-field levels of the ground state are equally populated, is given by

$$f_{ed} = \frac{8\pi^2 mc\nu}{3he^2(2J+1)}\frac{(n^2+2)^2}{9n}S_{ed}, \quad (1)$$

where $S_{ed} = e^2\sum_{\lambda=2,4,6}\Omega_\lambda(\Psi J\|U^\lambda\|\Psi' J')^2$ is the ED line strength, n is the linear refractive index of the medium, J is the total angular momentum quantum number of the ground state with $(2J+1)$ degeneracy, Ω_λ ($\lambda=2$, 4 and 6) are the JO intensity parameters, and $\|U^{(\lambda)}\|^2$ are the doubly reduced matrix elements evaluated in the intermediate coupling approximation for the transition $\Psi J \rightarrow \Psi' J'$. The Ω_λ parameters are obtained through a least squares fitting approach that gives the best fit between experimental and calculated oscillator strengths. The other constants have their usual meaning. Similarly, the MD oscillator strength is given by

$$f_{md} = \frac{8\pi^2 mc\nu}{3he^2(2J+1)}nS_{md}, \quad (2)$$

where $S_{md} = ((e^2h^2)/(16\pi^2m^2c^2))(\Psi J\|L+2S\|\Psi' J')^2$ is the MD line strength. The non-zero matrix elements will be those diagonal in the quantum numbers J, S, and L. Several important spectroscopic parameters can be obtained after the determination of Ω_λ, including the radiative probability rate of a given transition, $A_{rad}=A_{ED}+A_{MD}$, where $A_{ED}=(64\pi^4\nu^3/(3h(2J+1)))((n(n^2+2)^2)/9)S_{ed}$, and $A_{MD}=(64\pi^4\nu^3/(3h(2J+1)))n^3S_{md}$. The radiative lifetime of a level is given by $\tau_R=1/A_T$, where A_T is the total radiative transition probability for an excited state that is given by the summation of the A_{rad} terms over all the terminal states, and the branching ratio of each transition, $\beta_R=A_{rad}/A_T$.

As described elsewhere [41,42], the TL spectroscopy is based on a simple pump–probe setup. The TL effect is based on the heat deposition by nonradiative processes following optical energy absorption of a laser beam that produces heat. In this situation, a transverse temperature gradient is established and owing to the temperature dependence of the optical path length change, ds/dT (for solid samples), a lens-like optical element is created. The propagation of a probe laser beam through this pump-induced TL results in a variation of its on-axis intensity with respect to the non-pumped sample. If the pump is suddenly switched on, then

the on-axis intensity of the probe beam varies with time until it reaches a steady value. For this transient regime of the probe beam, an analytical expression for its on-axis intensity in the far-field was presented by Shen et al. [41], which is given by Eq. (2) in Ref. [42]. The fitting of the experimental transient with this analytical expression yields two parameters: the thermal diffusivity, D, by means of the TL characteristic signal response time ($t_c = w_{ex}^2/4D$, where w_{ex} is the radius of the excitation beam into the sample), and θ that is approximately the TL phase shift. θ divided by the absorbed pump power, P_{abs}, is given by

$$\Theta = -\frac{\theta}{P_{abs}} = \frac{1}{K\lambda_p}\frac{ds}{dT}\varphi \tag{3}$$

in which λ_p is the probe beam wavelength, $K = \rho c_p D$ is the thermal conductivity, ρ is the mass density, c_p is the specific heat, and φ is the fraction of absorbed energy converted into heat. This last parameter includes all information about luminescence and energy transfer and its equation is specific for each case (dopant ion, excitation, etc.). Therefore, through the knowledge of φ, it is possible to obtain the fluorescence quantum efficiency of emission levels. The term $C = (K\lambda_p)^{-1} ds/dT$ is in principle independent of the type of the dopant ion, i.e., it is a feature of the host.

4. Results and discussion

4.1. Y_2O_3:Eu^{3+} transparent ceramic

Fig. 1(a) shows the optical absorption spectrum of Y_2O_3:Eu transparent ceramic in the range of 300–700 nm along with the assignment of the bands. The absorption bands correspond to the

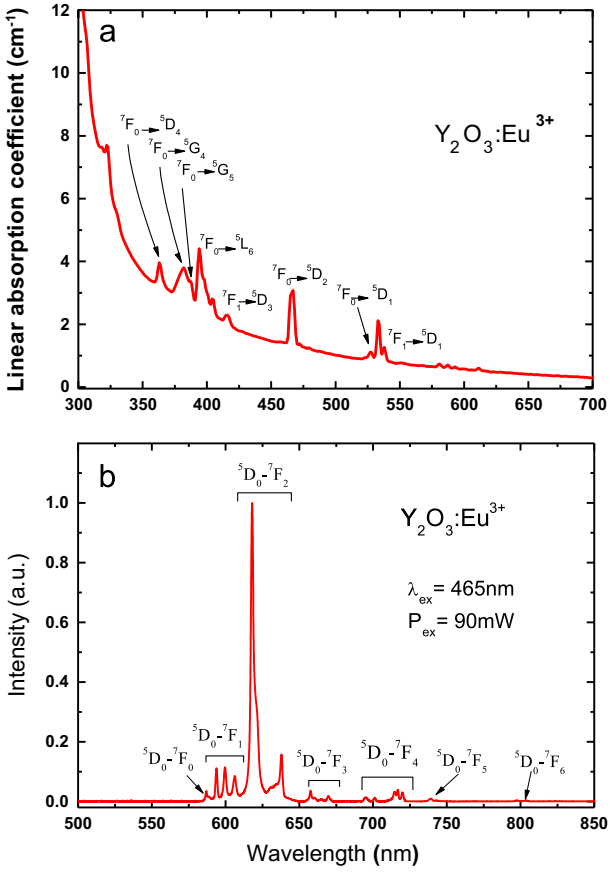

Fig. 1. (a) Linear absorption and (b) emission spectra of the 1.0 mol% Eu^{3+} doped Y_2O_3 ceramic.

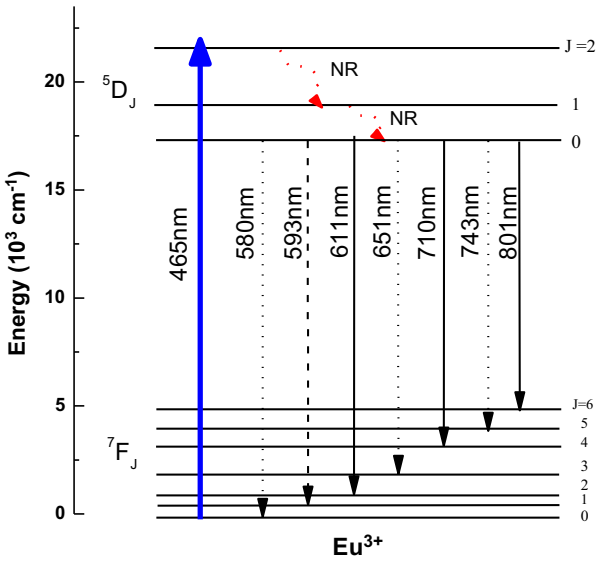

Fig. 2. Simplified energy levels diagram of 1.0 mol% Eu^{3+} doped Y_2O_3 ceramic. The solid lines indicate the allowed electric dipole (ED) transitions, the dash lines the allowed magnetic dipole (MD) transitions, and the dotted lines are prohibited ED and MD transitions.

Table 1
Transition wavelength, electro-dipole radiative rate, and branching ratio, as well as radiative and experimental lifetimes for Y_2O_3:Eu^{3+}.

$^5D_0 \rightarrow$	λ (nm)	A_{rad} (s^{-1})	β (%)	τ_{rad} (ms)	τ_{exp} (ms)
$^7F_0$	580	0	0	1.65	1.02
$^7F_1$	593	87.12	14.35		
$^7F_2$	611	488.67	80.47		
$^7F_3$	651	0	0		
$^7F_4$	710	29.12	4.79		
$^7F_5$	743	0	0		
$^7F_6$	801	2.39	0.39		

4f–4f optical excitations from the ground $^7F_0$ and thermally populated $^7F_1$ levels to the excited states of the Eu^{3+} ion. Absorption peaks at around 366, 382, 387, 394 and 467 nm correspond to the transitions from ground state $^7F_0$ to the excited states $^5D_4$, $^5G_4$, $^5G_2$, $^5L_6$, and $^5D_2$, respectively. The overlap of these transitions as well as the MD contribution makes the JO analysis inconclusive. An alternative way to obtain the Ω_λ ($\lambda = 2$, 4, and 6) parameters is from the analysis of the $^5D_0 \rightarrow {}^7F_J$ ($J = 0$–6) transitions in the emission spectrum (Figs. 1(b) and 2) [43,44]. Among these transitions, the $^5D_0 \rightarrow {}^7F_1$ transition is MD allowed and thus independent of the host matrix. The transitions $^5D_0 \rightarrow {}^7F_J$ ($J = 0$, 3, and 5) are prohibited both by ED and MD, whereas $^5D_0 \rightarrow {}^7F_J$ ($J = 2$, 4, and 6) are induced ED allowed and are affected by the host matrix. The $^5D_0$ level is non-radiatively populated from the 465 nm Ar laser-populated $^5D_2$ level, and generates all the emissions. Ω_λ can be calculated from the ratio of the intensity of the $^5D_0 \rightarrow {}^7F_J$ ($J = 2$, 4, and 6) transitions by means of the following equation [43–45]:

$$\frac{\int I_J d\upsilon}{\int I_1 d\upsilon} = \frac{A_J}{A_1} = \frac{e^2}{S_{MD,1}}\frac{\nu_J^3}{\nu_1^3}\frac{n(n^2+2)^2}{9n^3}\Omega_\lambda \langle \psi J \| U^\lambda \| \psi' J' \rangle^2 \tag{4}$$

where $S_{MD,1} = 9.6 \times 10^{-42}$ esu^2 cm^2 is the MD line strength of the $^5D_0 \rightarrow {}^7F_1$ transition of the Eu^{3+} ions [45] with frequency ν_1, A_J are radiative transition rate calculated using the A_{ED} expression above, $n = 1.82$ is the refractive index, ν_J ($J = 2$, 4, and 6) are the $^5D_0 \rightarrow {}^7F_J$ transition frequencies, and U_λ^2 are the reduced matrix element of the Eu^{3+} ion. Using the U_λ^2 values for LaF_3 [46], the values for the Ω_λ

parameters were obtained: $\Omega_2=6.89\times10^{-20}$, $\Omega_4=0.83\times10^{-20}$, and $\Omega_6=0.07\times10^{-20}$ cm^2, in agreement with the literature [47]. Further, the theoretical probability rate, branching ratio, and radiative lifetime are presented in Table 1.

The fluorescence decay of the $^5D_0$ level ($^5D_0\rightarrow{}^7F_2$ transition) of Eu^{3+} ions under excitation at 465 nm is shown in Fig. 3, together with the results of the best-fit analysis. A single exponential function was employed and a lifetime of $\tau_{exp}=1.02$ ms obtained, in excellent agreement with results from single crystals [47]. The fluorescence quantum efficiency, η, of this level was obtained by calculating the ratio $\eta=\tau_{exp}/\tau_{rad}=0.62$. For systems with only one emitting state, the fraction of absorbed energy converted into heat is given by $\varphi=1-\eta\lambda_{ex}/\langle\lambda_{em}\rangle=0.53$, in which $\lambda_{ex}=457$ nm and $\langle\lambda_{em}\rangle=613$ nm are respectively the excitation and average emission wavelengths.

Fig. 4(a) presents the TL signal obtained with 457 nm excitation wavelength with 295 mW incident power. From the best-fit of the experimental data (continuous line) using the TL equation from Ref. [42], the values of t_c and θ were obtained, further yielding $D=26\times10^{-3}$ cm^2/s, which is an average value obtained from several transients (Fig. 4(b)). This value is about half of the value reported for a 1 mol% Nd-doped Y_2O_3 single crystal, 59×10^{-3} cm^2/s [48,49].

Fig. 4(c) shows a linear behavior of θ versus the excitation power, with $\theta/P_{ex}=0.044$ W^{-1}. Since the linear absorption coefficient at the excitation wavelength of 457 nm is 1.437 cm^{-1}, it is possible to calculate the photo-thermal parameter $\Theta=0.43$ W^{-1} that together with φ provides the constant $C=0.82$ W^{-1}. Using the known values of the density ($\rho=5.03$ g/cm^3 [49]) and specific heat ($c_p=0.44$ J/g K [49]) of Y_2O_3, the thermal conductivity of the transparent ceramic $K=5.8$ W/m K was obtained. This value is lower than those reported in the literature for 1.0 mol% Nd-doped and 3.0 mol% Yb-doped Y_2O_3 single crystals that are around 13 W/m K [48–50]. The thermo-optical coefficient was determined to be $ds/dT=2.98\times10^{-6}$ K^{-1}, that is a promisingly low value when compared to other ceramics, crystals, and glasses [42,51]. This low ds/dT value, which is comparable only to those of phosphate glasses, makes this host an excellent nearly athermal material with potential for high power laser systems or to devices that require minimum optical distortion [52]. Another interesting characteristic is the near null value of the C constant. Since $C=(K\lambda_p)^{-1}ds/dT$, it is desirable for ds/dT to be near zero and K to be as large as possible in "athermal" systems, i.e., that C is close to zero. In this respect, the Y_2O_3 host presents better thermal properties than those of YAG ceramic and crystal, vanadate crystals, and fluorozirconate ZBLAN and aluminosilicate LSCAS glasses [42,53].

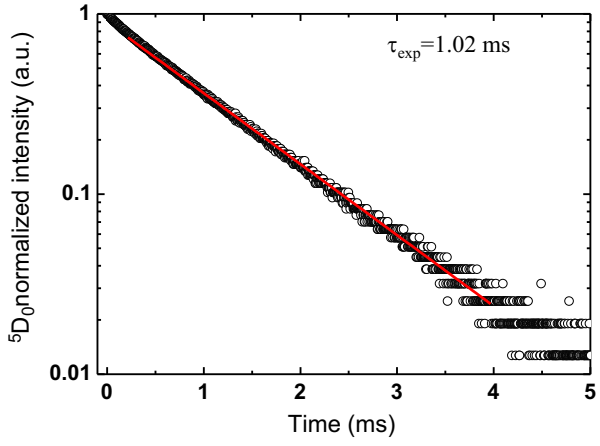

Fig. 3. Luminescence decay of the level $^5D_0$ for 1.0 mol% Eu^{3+} doped Y_2O_3 ceramic under excitation at 465 nm.

4.2. Y_2O_3:Tm^{3+} transparent ceramic

The absorption spectrum of the Y_2O_3:Tm transparent ceramic in the range of 320–2200 nm is shown in Fig. 5(a). The absorption peaks around 358, 463, 658, 684, 796, 1203, and 1635 nm correspond to the transitions from the ground state $^3H_6$ to the excited states $^1D_2$,$^1G_4$, $^3F_3$, $^3F_2$, $^3H_4$, $^3H_5$, and $^3F_4$, respectively. Using the Judd–Ofelt theory, the following JO parameters were obtained: $\Omega_2=2.47\times10^{-20}$, $\Omega_4=0.59\times10^{-20}$, and $\Omega_6=0.29\times10^{-20}$ cm^2, which are in agreement with the literature [54]. The emission spectrum under excitation at 465 nm is shown in Fig. 5(b) together with the assignment of the corresponding electronic transitions. Lifetimes were experimentally determined analyzing the emissions at around 665 and 800 nm under excitation at 476 nm. The emission decay from the $^3H_4$ level at around 800 nm ($^3H_4\rightarrow{}^3H_6$ transition; Fig. 6) is described by a single exponential function with a lifetime of 310 μs, as shown in Fig. 7(a). On the other hand, the emission decay around 665 nm (in principle from the $^1G_4\rightarrow{}^3F_4$ transition) incorporates a distribution of relaxation times (Fig. 7(b)) and could not be fitted with a single exponential function. Analysis with a double exponential function yielded lifetimes of 75 μs and 116 μs. The origin of this non-exponential character is explained in the simplified energy level diagram shown in Fig. 6, where two possible emission channels around 665 nm, namely transitions

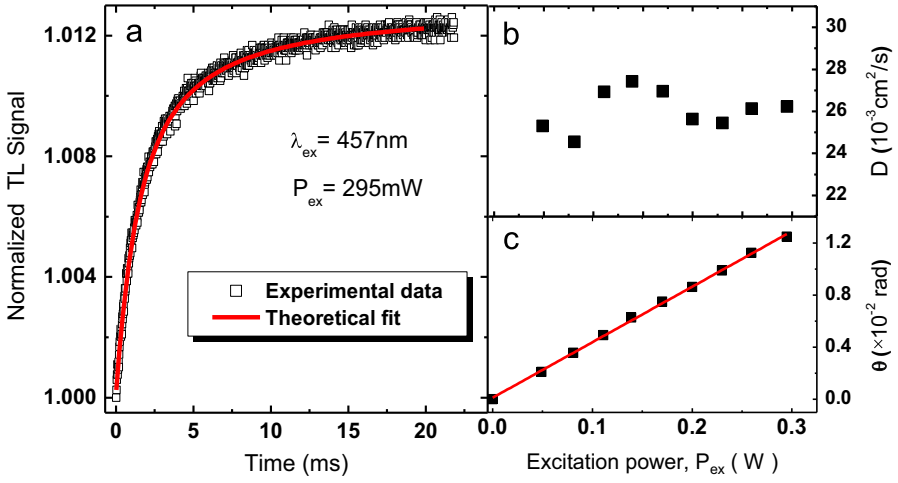

Fig. 4. (a) Normalized thermal lens signal, (b) thermal diffusivity, and (c) thermal lens phase shift versus the excitation power, for 1 mol% Eu^{3+} doped Y_2O_3 ceramic, under excitation at 457 nm.

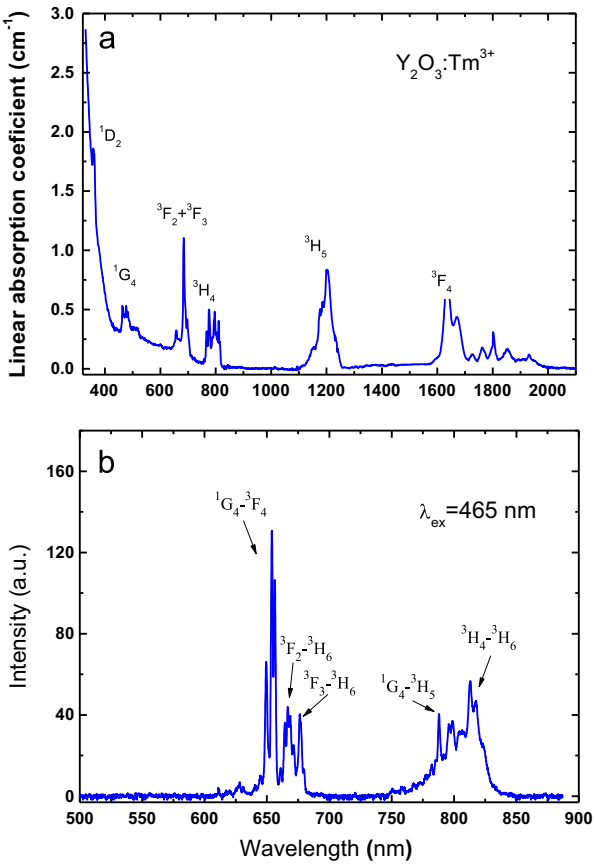

Fig. 5. (a) Linear absorption and (b) emission spectra for 0.5 mol% Tm^{3+} doped Y_2O_3 ceramic.

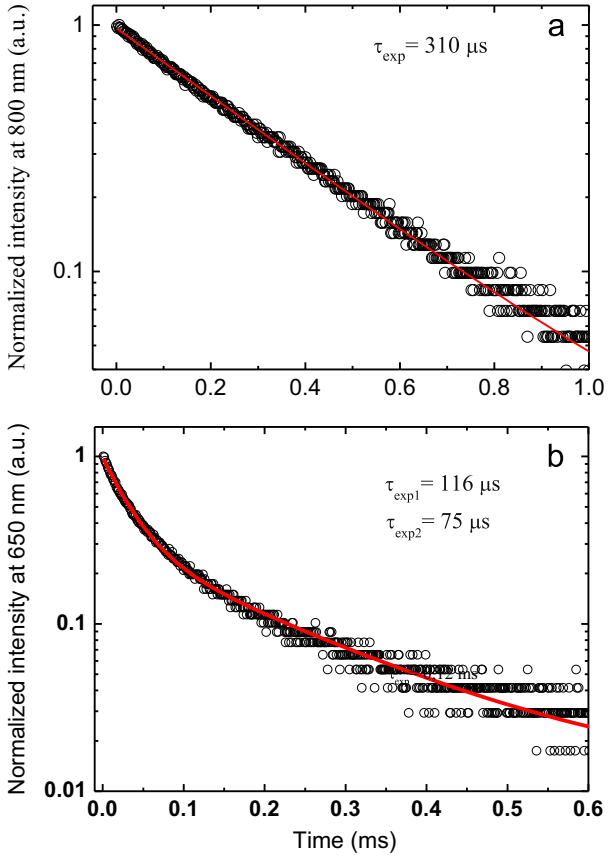

Fig. 7. Luminescence decays of the emissions at 650 and 800 nm for 0.5 mol% Tm^{3+} doped Y_2O_3 ceramic, under excitation at 476 nm.

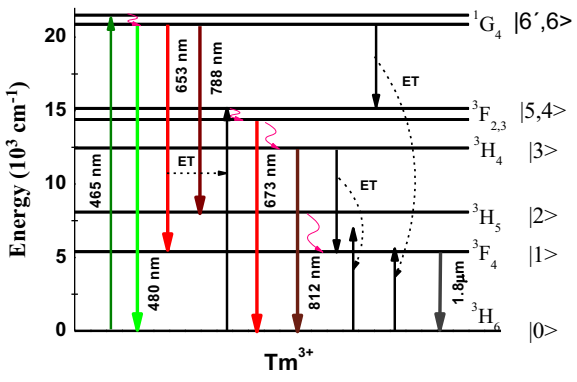

Fig. 6. Partial energy level diagram for Tm^{3+} ions under excitation at 465 nm, presenting the processes considered in formulating the rate equations.

Table 2
Transition wavelength, electro-dipole radiative rate, branching ratio, radiative lifetime, experimental lifetime, and fluorescence quantum efficiency for Y_2O_3:Tm^{3+}.

Transition	λ (nm)	A_{ed} (s^{-1})	β (%)	τ_{rad} (ms)	τ_{exp} (ms)	η
$^1G_4 \rightarrow {}^3H_6$	488	720.824	55.57	0.771	0.116	0.151
$^3F_4$	653	75.888	5.78			
$^3H_5$	788	329.223	25.38			
$^3H_4$	1159	142.591	10.99			
$^3F_3$	1500	22.176	1.71			
$^3F_2$	1640	6.444	0.57			
$^3F_2 \rightarrow {}^3H_6$	666	221.318	24.58	1.111	–	–
$^3F_4$	1060	572.069	63.53			
$^3H_5$	1470	94.620	10.51			
$^3H_4$	3920	12.418	1.38			
$^3F_3$	17,300	0.009	0			
$^3F_3 \rightarrow {}^3H_6$	673	879.627	75.42	0.857	0.075	0.088
$^3F_4$	1130	23.170	1.99			
$^3H_5$	1606	261.202	22.39			
$^3H_4$	5070	2.350	0.20			
$^3H_4 \rightarrow {}^3H_6$	812	745.182	90.07	1.209	0.310	0.256
$^3F_4$	1460	70.293	8.49			
$^3H_5$	2350	11.896	1.44			
$^3F_4 \rightarrow {}^3H_6$	1800	179.095		5.584	–	–

$^1G_4 \rightarrow {}^3F_4$ and $^3F_3 \rightarrow {}^3H_6$, are indicated. The shorter lifetime was attributed to the decay from the $^3F_3$ level due to the smaller energy gap between it and the next low level than in the case of the $^1G_4$ level.

Three prominent mechanisms of energy transfer involving the ground state and the levels $^1G_4$ and $^3H_4$, namely $^1G_4 \rightarrow {}^3F_4$:$^3H_6 \rightarrow {}^3F_2$, $^1G_4 \rightarrow {}^3F_2$:$^3H_6 \rightarrow {}^3F_4$, and $^3H_4 \rightarrow {}^3F_4$:$^3H_6 \rightarrow {}^3F_4$, are shown in Fig. 6, where the small wavy arrows represent multiphonon decay. The existence of more than one emitting electronic state requires the expression for the fraction of absorbed energy converted into heat (Eq. of φ) to be rewritten to take into account fluorescence quantum efficiencies of the emitting levels, the several excitation and emission wavelengths, and the energy transfer rates. The heat generated per unit of time and volume, Q, considering these transitions is

$$\begin{aligned} Q = {} & R_p n_0 (E_{ex} - E_{06'}) + W^{mp}_{6'6} n_{6'} (E_{6'0} - E_{60}) \\ & + W^{ET}_{65} n_6 (E_{65} - E_{01}) + W^{ET}_{61} n_6 (E_{61} - E_{05}) \\ & + W^{mp}_{54} n_5 (E_{50} - E_{40}) + W^{mp}_{43} n_4 (E_{40} - E_{30}) \\ & + W^{ET}_{31} n_3 (E_{31} - E_{01}) + W^{mp}_{21} n_2 E_{21} + W^{mp}_{10} n_1 E_{10}, \end{aligned} \quad (5)$$

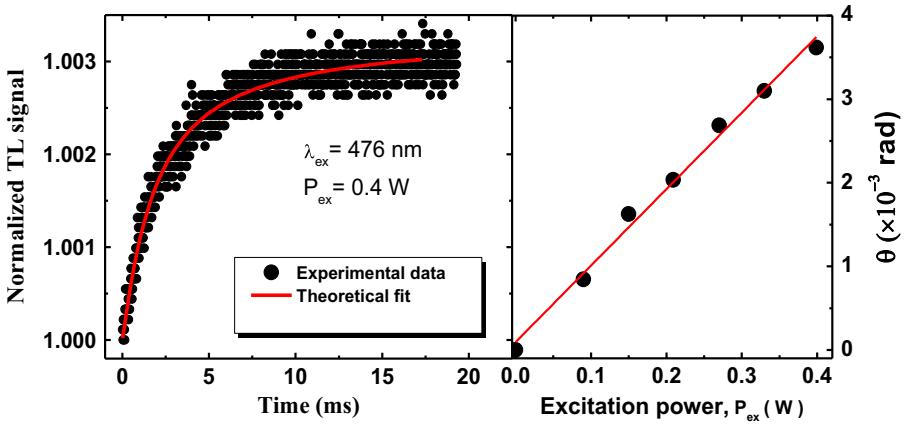

Fig. 8. Normalized thermal lens signal and thermal lens phase shift versus the excitation power, for 0.5 mol% Tm^{3+} doped Y_2O_3 ceramic, under excitation at 476 nm.

where E_{ij} is the energy difference between levels i and j, R_p is the pumping rate, W_i^{ET} is the energy transfer rate from level i, W_{ij}^{mp} is the multiphonon decay rate from level i to level j, and n_i is the population of the ith level. The population dynamics of the Tm^{3+} levels are described, considering the labeling in Fig. 6, by the following system of rate equations:

$$\frac{dn_{6'}}{dt} = R_p n_0 - W_{6'6}^{mp} n_{6'} \tag{6.a}$$

$$\frac{dn_6}{dt} = W_{6'6}^{mp} n_{6'} - n_6/\tau_6 \tag{6.b}$$

$$\frac{dn_5}{dt} = \left(W_{61}^{ET} + W_{65}^{ET}\right) n_6 - W_{54}^{mp} n_5 \tag{6.c}$$

$$\frac{dn_4}{dt} = W_{54}^{mp} n_5 - n_4/\tau_4 \tag{6.d}$$

$$\frac{dn_3}{dt} = W_{43}^{mp} n_4 - n_3/\tau_3 \tag{6.e}$$

$$\frac{dn_2}{dt} = W_{62}^{rad} n_6 - W_{21}^{mp} n_2 \tag{6.f}$$

$$\frac{dn_1}{dt} = 2W_{31}^{ET} n_3 + \left(W_{61}^{ET} + W_{65}^{ET}\right) n_6 + W_{21}^{mp} n_2 + W_{61}^{rad} n_6 - n_1/\tau_1 \tag{6.g}$$

with n_1–n_6 representing the population of electronic levels $^3F_4$, $^3H_5$, $^3H_4$, $^3F_2$, $^3F_3$, and $^1G_4$, in order, and W_{ij}^{rad} the radiative transition from level i to j, and A_i is the total radiative rate of the level i. In addition, the following relations are considered: $\tau_6^{-1} = A_6 + W_6^{ET}$, $\tau_4^{-1} = A_4 + W_{43}^{mp}$, $\tau_3^{-1} = A_3 + W_3^{ET}$, $A_6 = W_{60}^{rad} + W_{61}^{rad} + W_{62}^{rad}$, $W_6^{ET} = W_{65}^{ET} + W_{61}^{ET}$, $W_6^{ET}\tau_6 = \eta_6^{TE} = 1 - \eta_6 = 1 - (\tau_6/\tau_6^{rad})$, $W_{43}^{mp}\tau_4 = \varphi_4 = 1 - \eta_4$, $W_{31}^{TE}\tau_3 = \eta_3^{TE} = 1 - \eta_3 = 1 - (\tau_3/\tau_3^{rad})$, $W_{10}^{mp}\tau_1 = 1 - \eta_1$. From the steady state solutions of the rate equations and using the definitions above, the following equation for Q was found:

$$\begin{aligned} Q = R_p n_0 E_{ex}\Big[& 1 - \eta_6 \tfrac{E_{60}}{E_{ex}} - \eta_4(1-\eta_6)\tfrac{E_{40}}{E_{ex}} \\ & - \eta_3(1-\eta_6)(1-\eta_4)\frac{E_{30}}{E_{ex}} - 2\eta_1(1-\eta_6)(1-\eta_4)(1-\eta_3)\frac{E_{10}}{E_{ex}} \\ & + \tau_6 W_{62}^{rad}\frac{E_{21}}{E_{ex}} + (1-\eta_1)\tau_6 W_{60}^{rad}\frac{E_{10}}{E_{ex}}\Big]. \end{aligned} \tag{7}$$

The equation for the thermal load can be obtained from Eq. (7) through $\varphi = Q/R_p n_0 E_{ex}$, resuting in

$$\begin{aligned} \varphi = 1 & - \eta_6\frac{\lambda_{ex}}{\lambda_{60}} - \eta_4(1-\eta_6)\frac{\lambda_{ex}}{\lambda_{40}} - \eta_3(1-\eta_6)(1-\eta_4)\frac{\lambda_{ex}}{\lambda_{30}} \\ & - 2\eta_1(1-\eta_6)(1-\eta_4)(1-\eta_3)\frac{\lambda_{ex}}{\lambda_{10}} \\ & + \eta_{62}\frac{\lambda_{ex}}{\lambda_{21}} + \eta_{60}(1-\eta_1)\frac{\lambda_{ex}}{\lambda_{10}} \end{aligned} \tag{8}$$

where $\eta_{62} = \tau_6 W_{62}^{rad}$ and $\eta_{60} = \tau_6 W_{60}^{rad}$ are the radiative quantum efficiencies of the transitions 6→2 and 6→0, respectively. Using the JO theory and the measured luminescence decays, the fluorescence quantum efficiencies of levels $^3F_3$ and $^3H_4$ of Tm^{3+} were obtained. Table 2 shows the radiative lifetime for the transitions, branching ratio, experimental lifetimes, and the quantum efficiencies of several energy levels as $\eta_6 = 0.151$, $\eta_3 = 0.256$, $\eta_4 = 0.088$, $\eta_{62} = 0.038$ and $\eta_{60} = 0.084$. Since all other parameters are known, except the fluorescence quantum efficiency of the level $^3F_4$ emitting at ~1800 nm (η_1), Eq. (8) becomes $\varphi = 0.716 - 0.32\eta_1$, that can be used to obtain η_1 if φ is known. It should be noted that this equation is valid only for the investigated Tm concentration.

Fig. 8(a) presents a normalized TL signal for the Y_2O_3:Tm sample under excitation at 476 nm and for an excitation power of 400 mW. The TL phase shift versus the pumping power is shown in Fig. 8(b), where a linear behavior was observed with a linear fitting $\theta/P_{ex} = 0.0097\ W^{-1}$. The linear absorption coefficient of the Y_2O_3:Tm sample at 476 nm is 0.532 cm^{-1}, and so the parameter $\Theta_{Tm} = 0.365\ W^{-1}$ was evaluated. Using $C = 0.816\ W^{-1}$ obtained previously from the Y_2O_3:Eu sample, we calculated the thermal load $\varphi = 0.447$ for this Tm-doped sample. With this value, the fluorescence quantum efficiency of the level emitting at 1800 nm was estimated to be $\eta_1 = 0.84$ that is relatively high for a level with possible energy migration as is the case of $^3F_4$.

5. Conclusions

The optical characterization of Y_2O_3 transparent ceramics singly-doped with Eu^{3+} and Tm^{3+} was carried out. Traditional spectroscopic analysis and the use of the Judd–Ofelt theory were combined with thermal lens results to yield a number of optical and thermal properties of these ceramics. These measurements made if possible to obtain the thermal properties of the Y_2O_3 ceramic matrix in terms of thermal diffusivity $D = 26 \times 10^{-3}\ cm^2/s$, thermal conductivity $K = 5.8$ W/m K, and temperature coefficient of the optical path change $ds/dT = 3.0 \times 10^{-6}\ K^{-1}$. The thermal conductivity of the Y_2O_3:Eu ceramic was determined to be about half of the value of similar single-crystals, and the small temperature coefficient of the optical path length change suggests that these ceramics suitable for applications requiring nearly athermal response. Fluorescence quantum efficiencies of several levels, particularly 62% for the $^5D_0$ level of Eu^{3+} and 84% for the $^3F_4$ level of Tm^{3+}, were determined.

Acknowledgments

This work was supported by Brazilian Agencies FAPEAL (Project PRONEX-NEXO no. 2009-09-006), FINEP (Financiadora de Estudos e Projetos), CNPq (Conselho Nacional de Desenvolvimento Científico e Tecnológico, grant INCT NANO(BIO)SIMES), and CAPES (Coordenadoria de Aperfeiçoamento de Pessoal de Ensino Superior, Project PVE A077/2013). P.Y Poma is a graduate student supported by CAPES. Dr. KUK was supported by a Post Doctoral Fellowship grant of the Programa Nacional de Pós-Doutoramento (PNPD/CAPES) at the Universidade Federal de Alagoas (UFAL) through Project no. 02727/09-9. Currently Dr. KUK is a post-doctorate of Project PVE A077/2013. This material is based upon work supported by the National Science Foundation under Grant no. 1207080.

References

[1] P. Dorenbos, J. Lumin. 91 (2000) 155.
[2] C. Jacinto, A. Benayas, T. Catunda, J. Garcia-Sole, A.A. Kaminskii, D. Jaque, J. Chem. Phys. 129 (2008) 104705.
[3] A.S.S. de Camargo, C. Jacinto, L.A.O. Nunes, T. Catunda, D. Garcia, E.R. Botero, J.A. Eiras, J. Appl. Phys. 101 (2007) 053111.
[4] E.E. Brown, U. Hömmerich, A. Bluiett, C. Kucera, J. Ballato, S. Trivedi, J. Am. Ceram. Soc. 97 (2014) 2105.
[5] J.F. Bisson, H. Yagi, T. Yanagitani, A. Kaminskii, Y.N. Barabanenkov, K.I. Ueda, Opt. Rev. 14 (2007) 1.
[6] R.L. Coble, US Patent No. 3026210, USA, 1962.
[7] R.L. Coble, J. Appl. Phys. 32 (1961) 787.
[8] G.C. Wei, J. Phys. D: Appl. Phys. 38 (2005) 3057.
[9] P.J. Patel, G.A. Gilde, P.G. Dehmer, J.W. McCauley, Inorg. Opt. Mater. II 4102 (2000) 1.
[10] V. Lupei, A. Lupei, A. Ikesue, Opt. Mater. 30 (2008) 1781.
[11] J. Li, Y. Pan, Y. Zeng, W. Liu, B. Jiang, J. Guo, Int. J. Refract. Met. Hard Mater. 39 (2013) 44.
[12] C. Greskovich, S. Duclos, Annu. Rev. Mater. Sci. 27 (1997) 69.
[13] D.A. Casano, C.D. Greskovich, and F.A. Dibianca, US Patent No. 4421671-A, General Electric Co., 1984.
[14] Y. Ito, H. Yamada, M. Yoshida, H. Fujii, G. Toda, H. Takeuchi, Y. Tsukuda, Jpn. J. Appl. Phys. Part 2: Lett. 27 (1988) L1371.
[15] M. Yoshida, M. Nakagawa, H. Fujii, F. Kawaguchi, H. Yamada, Y. Ito, H. Takeuchi, T. Hayakawa, Y. Tsukuda, Jpn. J. Appl. Phys. Part 2: Lett. 27 (1988) L1572.
[16] D.A. Cusano, C.D. Greskovich, and F.A. Dibianca, US Patents Nos. EP97295-A; JP59030883-A; US4466930-A; US4518545-A; IL68641-A; EP97295-B; DE33-69004-G; JP88059436-B, General Electric Co., 1984.
[17] D.A. Cusano, C.D. Greskovich, and F.A. Dibianca, US Patents Nos. EP97296-A; JP59030882-A; US4466929-A; US4473513-A; IL68676-A; EP97296-B; DE3368773-G; US4747973-A; JP88059435-B; JP1038491-A; JP90062596-B General Electric Co., 1984.
[18] A. Ikesue, T. Kinoshita, K. Kamata, K. Yoshida, J. Am. Ceram. Soc. 78 (1995) 1033.
[19] A.A. Kaminskii, Laser Photonics Rev. 1 (2007) 93.
[20] A. Ikesue, Y.L. Aung, Nat. Photonics 2 (2008) 721.
[21] A. Ikesue, K. Kamata, J. Ceram. Soc. Jpn. 103 (1995) 1155.
[22] N. Saito, S. Matsuda, T. Ikegami, J. Am. Ceram. Soc. 81 (1998) 2023.
[23] J.Q. Wang, S.H. Zheng, Y.L. Yue, Z.D. Tao, X.D. Sun, J. Inorg. Mater. 18 (2003) 1222.
[24] L. Wen, X.D. Sun, L. Qi, G.X. Xu, J. Inorg. Mater. 21 (2006) 539.
[25] A.V. Belyakov, D.O. Lemeshev, E.S. Lukin, G.P. Val'nin, E.E. Grinberg, Glass Ceram. 63 (2006) 262.
[26] K. Serivalsatit, B.Y. Kokuoz, B. Kokuoz, J. Ballato, Opt. Lett. 34 (2009) 1033.
[27] K. Serivalsatit, B. Kokuoz, B. Yazgan-Kokuoz, M. Kennedy, J. Ballato, J. Am. Ceram. Soc. 93 (2010) 1320.
[28] A. Ferrier, C.W. Thiel, B. Tumino, M.O. Ramirez, L.E. Bausa, R.L. Cone, A. Ikesue, P. Goldner, Phys. Rev. B 87 (2013) 041102.
[29] R.P. Yavetskiy, V.N. Baumer, M.I. Danylenko, A.G. Doroshenko, I.N. Ogorodnikov, I.A. Petrusha, A.V. Tolmachev, V.Z. Turkevich, Ceram. Int. 40 (2014) 3561.
[30] A. Fukabori, T. Yanagida, J. Pejchal, S. Maeo, Y. Yokota, A. Yoshikawa, T. Ikegami, F. Moretti, K. Kamada, J. Appl. Phys. 107 (2010) 073501.
[31] A. Fukabori, V. Chani, K. Kamada, F. Moretti, A. Yoshikawa, Cryst. Growth Des. 11 (2011) 2404.
[32] A. Fukabori, L. An, A. Ito, V. Chani, K. Kamada, A. Yoshikawa, T. Ikegami, T. Goto, Ceram. Int. 38 (2012) 2119.
[33] Y. Futami, T. Yanagida, Y. Fujimoto, J. Pejchal, M. Sugiyama, S. Kurosawa, Y. Yokota, A. Ito, A. Yoshikawa, T. Goto, Radiat. Meas. 55 (2013) 136.
[34] R. Ramaseshan, S. Sundarrajan, R. Jose, S. Ramakrishna, J. Appl. Phys. 102 (2007) 111101.
[35] N.R. Prasad, W.C. Edwards, S.B. Trived, S.W. Kutcher, C.-C. Wang, J.-S. Kim, U. Hömmerich, V. Shukla, R. Sadangi, B.H. Kear, IEEE J. Sel. Top. Quantum Electron. 13 (2007) 831.
[36] I.W. Chen, X.H. Wang, Nature 404 (2000) 168.
[37] W.T. Carnall, in: K.A. Gschneidner Jr., L. Eyring (Eds.), Handbook on the Physics and Chemistry of Rare Earths, 4, North-Holland, Amsterdam, 1979.
[38] S. Hüfner, Optical Spectra of Transparent Rare Earth Compounds, Academic Press, New York, 1978.
[39] B.R. Judd, Phys. Rev. 127 (1962) 750.
[40] G.S. Ofelt, J. Chem. Phys. 37 (1962) 511.
[41] J. Shen, R.D. Lowe, R.D. Snook, Chem. Phys. 165 (1992) 385.
[42] C. Jacinto, D.N. Messias, A.A. Andrade, S.M. Lima, M.L. Baesso, T. Catunda, J. Non-Cryst. Solids 352 (2006) 3582.
[43] D.U. Maheswari, J.S. Kumar, L.R. Moorthy, K. Jang, and M. Jayasimhadri, Physica B: Condens. Matter 403 (2008) 1690.
[44] A.F. Adadurov, P.N. Zhmurin, V.N. Lebedev, V.N. Kovalenko, Funct. Mater. 18 (2011) 315.
[45] M.H.V. Werts, R.T.F. Jukes, J.W. Verhoeven, Phys. Chem. Chem. Phys. 4 (2002) 1542.
[46] L. Liu, X. Chen, Nanotechnology 18 (2007) 255704.
[47] M.J. Weber, Phys. Rev. 171 (1968) 283.
[48] P.H. Klein, J. Appl. Phys. 38 (1967) 1598.
[49] J.H. Mun, A. Jouini, A. Novoselov, A. Yoshikawa, T. Fukuda, J. Ceram. Process. Res. 12 (2011) 169.
[50] V. Peters, A. Bolz, K. Petermann, G. Huber, J. Cryst. Growth 237 (2002) 879.
[51] A.A. Andrade, T. Catunda, I. Bodnar, J. Mura, M.L. Baesso, Rev. Sci. Instrum. 74 (2003) 877.
[52] N.G.C. Astrath, M.J. Barboza, A.N. Medina, A.C. Bento, M.L. Baesso, W.F. Silva, C. Jacinto, T. Catunda, J. Appl. Phys. 106 (2009) 073511.
[53] D.N. Messias, C. Jacinto, M.J.V. Bell, T. Catunda, IEEE J. Quantum Electron. 43 (2007) 751.
[54] Q. Yi, S. Zhou, T. Tsuboi, H. Lin, and H. Teng, Pacific Rim Laser Damage 2011: Optical Materials for High Power Lasers 8206 (2012) 82061U.